

LETTER TO THE EDITOR

# Transient star B/R ratio and star formation in $z \gtrsim 1$ lensed galaxies

Sung Kei Li <sup>\*1</sup>, Jose M. Palencia<sup>2</sup>, Jose M. Diego<sup>2</sup>, Jeremy Lim<sup>1</sup>, Patrick L. Kelly<sup>3</sup>, Ashish K. Meena<sup>4</sup>, James Nianias<sup>1</sup>, Hayley Williams<sup>3</sup>, Liliya L.R. Williams<sup>3</sup>, and Adi Zitrin<sup>4</sup>

<sup>1</sup> Department of Physics, The University of Hong Kong, Pokfulam Road, Hong Kong

<sup>2</sup> Instituto de Física de Cantabria (CSIC-UC), Avda. Los Castros s/n, 39005 Santander, Spain

<sup>3</sup> Minnesota Institute for Astrophysics, University of Minnesota, 116 Church St. SE, Minneapolis, MN 55455, USA

<sup>4</sup> Department of Physics, Ben-Gurion University of the Negev, PO Box 653, Be'er-Sheva 8410501, Israel

June 24, 2025

## ABSTRACT

The extreme magnification from galaxy clusters and microlenses therein allows the detection of individual, luminous stars in lensed galaxies as transient events, and hence provides a valuable window into the high mass stellar population in  $z > 1$  galaxies. As these bright stars can only be formed at specific ages, the relative abundance of transient events at blue (B) and red (R) optical wavelengths ( $B/R$  ratio) can provide insights into the star formation history of lensed galaxies. Here, we forward model the transient detection rates in an idealized mock scenario to find that the  $B/R$  ratio of strongly lensed  $z > 1$  galaxies decreases quickly with increasing age. This ratio has comparatively low sensitivity to metallicity and dust attenuation, with no significant dependency on the stellar initial mass function. As a proof-of-concept, we show that a simple starburst cannot simultaneously fit the  $B/R$  and spectral energy distribution of the “Warhol” arc ( $z = 0.94$ ), indicating a more complex (recent) star formation history. Although limited only to lensed higher redshift galaxies in cluster fields, this result shows that the transient  $B/R$  ratio could be used as an additional, complementary constraint on the star formation history of higher redshift galaxies in future works.

**Key words.** Gravitational lensing: strong – Gravitational lensing: micro – Galaxies: star formation

## 1. Introduction

Individual stars in lensed galaxies at  $z \gtrsim 1$  are now being routinely discovered in deep, repeated *Hubble Space Telescope* (HST) and *James Webb Space Telescope* (JWST) imaging of galaxy clusters (e.g., Kelly et al. 2018; Chen et al. 2019; Kelly et al. 2022; Yan et al. 2023; Meena et al. 2023; Fudamoto et al. 2025). These lensed stars must be intrinsically luminous, and be subject to extreme magnifications — from a combination of cluster macro- and stellar microlensing — to overcome the cosmological distance modulus and be detected as transient events (Miralda-Escude 1991; Oguri et al. 2018; Diego 2019). The two primary populations that constitute the lensed stars are: (i) the blue supergiants (BSGs, effective temperature of 10,000 – 30,000 K), which can be seen in blue filters that probe the restframe UV/optical (e.g., Kelly et al. 2018); and (ii) red supergiants (RSGs, effective temperature of 3000 – 4000 K) which can be seen in red filters that cover the restframe NIR (Diego et al. 2023). Bright O/B stars, or other classes of evolved stars, such as asymptotic giant branches and Cepheid variables (Diego et al. 2024a) should also be detected as lensed transients, albeit much less frequently, given their lower luminosity.

Massive stars are always very short-lived and so are only present in stellar populations at specific ages. For example, BSGs can only exist in stellar populations having ages  $\lesssim 10$  Myr. The relative abundance of massive BSGs and RSGs has been well explored in nearby galaxies (where resolved photometry can be carried out) to characterize properties, such as the age and metallicity, of the stellar populations therein (Eggenberger et al. 2002; Dohm-Palmer & Skillman 2002). As lensing is achromatic

and does not affect the color of lensed stars, the ratio between the detection rate of transients in a blue filter to a red filter,  $B/R$ , should also directly correlate to the abundance of the corresponding stellar populations in the lensed galaxy to the first order, albeit the fact that the maximum magnification RSGs can attain is lower owing to their larger radius. Diego et al. (2024b) first investigated how the  $B/R$  ratio is related to the relative abundance of RSG and BSG in a lensed galaxy under a simplified scenario, and found that a roughly equivalent abundance of BSG and RSG can reproduce the observed  $B/R$  ratio. In light of the strong dependency between the presence of BSGs/RSGs and age, the  $B/R$  ratio can provide insights into the underlying star formation history.

In this letter, we explore how the lensed star  $B/R$  ratio depends on various star formation parameters and how this can provide insights into the properties of underlying stellar populations. We adopt the AB magnitude system (Oke & Gunn 1983), along with standard cosmological parameters:  $\Omega_m = 0.3$ ,  $\Omega_\Lambda = 0.7$ , and  $H_0 = 70 \text{ km s}^{-1} \text{ Mpc}^{-1}$ .

## 2. Transient Detection Rate

As a demonstration, we use a lensed arc known as “Warhol” ( $z = 0.94$ ) in which multiple transients have been detected over the last decade (Chen et al. 2019; Kelly et al. 2022; Yan et al. 2023). We adopt the magnification map of Warhol from Palencia et al. (2025), where for each pixel in which light from Warhol was detected, we have a specific tangential magnification  $-10^{4.7} < \mu_t < 10^4$  radial magnification,  $1.7 < \mu_r < 2.3$ , and surface mass density of stellar microlenses  $30 < \Sigma_\star < 115 M_\odot/\text{pc}^2$ .

\* keihk98@connect.hku.hk

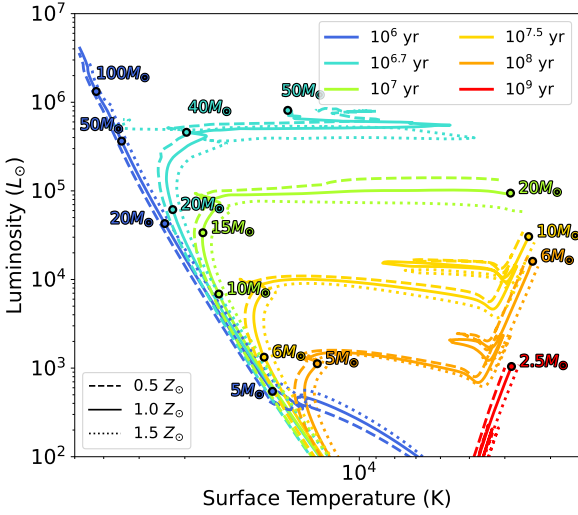


Fig. 1: Subsets of MIST age isochrone (Choi et al. 2016) used in our SPISEA (Hosek et al. 2020) stellar population synthesis featuring a range of ages as shown in the legend. The metallicity of each of the subsets is reflected by their linestyle as shown in the bottom legend. All of them have no dust extinction, where the color represents the age of the isochrone as shown in the top legend. For each age isochrone, we also annotate some characteristic masses to indicate the mass-age dependency.

We begin by simulating stellar populations at different ages ( $t$ ), metallicities ( $Z_\star$ ), and dust extinctions ( $A_V$ ) with a modified stellar population synthesis code SPISEA (Hosek et al. 2020) that adopts a MIST isochrone (Choi et al. 2016) and either a Kroupa (2001) or a Top-heavy stellar initial mass function (IMF, high mass power-law slope of  $-2.3$  and  $-1$ , respectively). A subset of the age isochrones used is shown in Fig. 1 for reference. Each of the stellar populations simulated has the same total stellar mass of  $10^6 M_\odot$ . To ensure our simulated populations are statistically representative, we drew each stellar population from the underlying IMF multiple times.

Following the methodology in Li et al. (2025) and Palencia et al. (2025), we evaluate the expected number of transients detected in any given observation by calculating the expected number of stars in a stellar population that is brighter than the detection threshold when subject to cluster macro-lensing and stellar micro-lensing. The probability of any stars having some magnification,  $p(\mu)$ , is characterized by  $\mu_t$ ,  $\mu_r$ , and  $\Sigma_\star$  (Palencia et al. 2024). To ensure the unresolved objects in the lensed arcs are individual stars, we demand that they must be detected in the form of transients, such that our sample would not be contaminated by persistent unresolved objects that vary in brightness, such as star clusters (e.g., Li et al. 2024). We hence adopt the detectable through microlensing (DTM) limit Diego et al. (2024c) in our calculation, restricting the individual background lensed stars to be undetectable when subjected to cluster macro magnification only, but becoming temporarily detectable when they are additionally boosted in magnification by microlenses. Mathematically, the detection rate for any pixel that has  $\mu_t$ ,  $\mu_r$ , and  $\Sigma_\star$ , is given by:

$$\mathcal{R}_f(\mu_t, \mu_r, \Sigma_\star; t, Z_\star, A_V) \propto \frac{1}{\mu_t \mu_r} \int_{-\infty}^{m_{\sigma,f}} \int_{\mu_{\min}=10^{-1}}^{\mu_{\max}=10^4} d\mu d\mu'_f p(\mu; \mu_t, \mu_r, \Sigma_\star) N_f(m - 2.5 \log_{10} \mu; t, Z_\star, A_V), \quad (1)$$

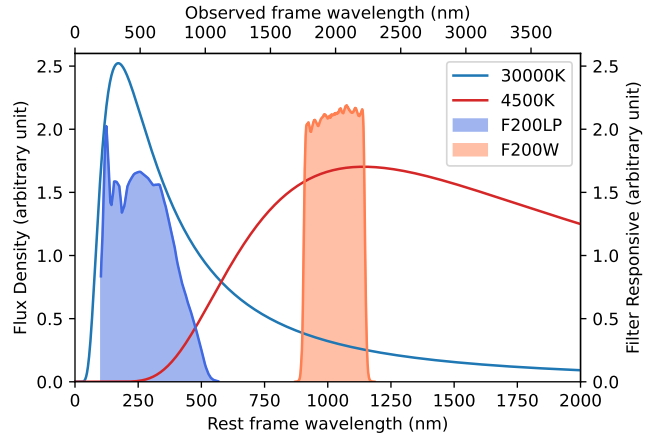


Fig. 2: Filter response curve of *HST* F200LP (blue shade) and *JWST* F200W (coral shade), and the black body spectrum of two stars at 30000 K (blue curve) and 4500 K (red curve) — characteristic temperature of BSGs and RSGs, respectively — shown at the rest frame and observed frame ( $z = 0.94$ ) wavelengths. One can see that the two filters best capture the brightest part of the black body of the two classes of stars.

where  $m_{\sigma,f}$  denotes the detection limit in apparent magnitude  $m$  at filter  $f$ . By convolving  $p(\mu; \mu_t, \mu_r, \Sigma_\star)$  with the stellar luminosity function  $N_f(m; t, Z_\star, A_V)$  for a stellar population at a given age, metallicity and dust extinction, we can compute the expected number of lensed stars and their brightness distribution after considering all possible lensing magnifications they can attain,  $\mu$ , through the second integral. The choice of  $\mu_{\min}$  and  $\mu_{\max}$  in this integral is motivated by the  $p(\mu)$  resolution and maximum size of lensed stars, respectively (Palencia et al. 2024; Li et al. 2025). The first integral determines the expected number of stars that are brighter than the detection threshold and made detectable given any random observation after accounting for lensing magnification. The whole process is computed over every pixel in the image plane representing the arc, requiring us to divide the pixel area by the macro-magnification  $\mu_t \mu_r$  to account for the decrease in source plane area. We assume a constant surface brightness in the lensed arc for simplicity, which might vary by a factor of  $\sim 5$  in real arcs, with diminished variations in regions over which transients are usually detected (near the critical curve).

We select two characteristic filters that best capture the light from BSGs and RSGs at  $z \approx 1$ . For the blue filter, we choose the *HST* WFC3/UVIS F200LP as it spans the rest-frame UV through optical (100 nm to 540 nm) and has the highest sensitivity to BSGs; for the red filter, we choose the high-throughput *JWST* NIRCAM F200W as it covers rest-frame NIR (850 nm to  $1.2 \mu\text{m}$ ) where RSGs are the brightest. Due to the high sensitivity of this filter, it is used in many deep programs. The filter response curves and characteristic blackbody spectra of BSGs and RSGs are shown in Fig. 2. We adopt a detection limit of  $30 m_{AB}$  for F200LP, and  $29.7 m_{AB}$  for F200W, as motivated by the *HST* Flashlights survey (Kelly et al. 2022) and *JWST* PEARLS program (Windhorst et al. 2023; Williams in prep.). Notice that BSGs can sometimes be detected in F200W, and conversely, RSGs can also be detected in F200LP. The likelihood of such detection, however, is low given the bandpasses of the respective filters compared with the blackbody spectra of the different stars. An example of the transient detection rate in these two filters is shown in Fig. 3, and that for other combinations of metallicity and dust is shown in Fig. A.1.

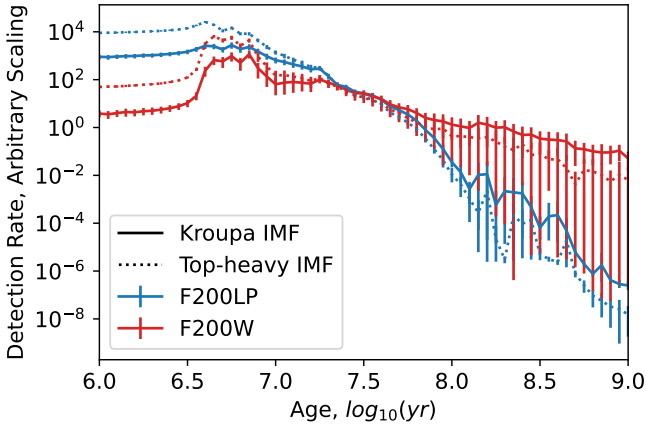


Fig. 3: Transient detection rate per unit mass for stellar populations at different ages with metallicity of  $0.5Z_{\odot}$  and  $A_V = 0$ , calculated with Eq. 1 under the magnification map of Warhol from Palencia et al. (2025). Blue curves show the detection rate in the *HST* F200LP filter (detection limit of  $30 m_{AB}$ ); red curves show the detection rate in the *JWST* F200W filter (detection limit of  $29.7 m_{AB}$ ). Solid and dotted lines show the case for a Kroupa IMF and a top-heavy IMF, respectively.

The transient  $B/R$  ratio for any given stellar population is then just the ratio between the detection rate summed over all the  $n$  lens model pixels that represent the arc in the two filters:

$$B/R = \frac{\sum_i^n \mathcal{R}_{F200LP}(\mu_{t,i}, \mu_{r,i}, \Sigma_{\star,i})}{\sum_i^n \mathcal{R}_{F200W}(\mu_{t,i}, \mu_{r,i}, \Sigma_{\star,i})} \quad (2)$$

We show the  $B/R$  ratio at different ages,  $Z_{\star}$ , and  $A_V$  in Fig. 4.

### 3. Result and Discussion

The transient detection rate per unit mass at  $z \approx 1$  in either blue (*HST* F200LP) or red (*JWST* F200W) filters is highest for star formation episodes in the most recent  $\sim 10$  Myr (notice the peak is delayed in the Red filter in Fig. 3, as massive stars take time to evolve into RSGs). Beyond  $\sim 10$  Myr, the rate decreases quickly with increasing age as shown in Fig. 3 because most BSGs and RSGs ( $\gtrsim 10^4 L_{\odot}$ ) only survive up to  $\sim 10$  Myr as shown in Fig. 1. After this age, transients detected are mostly associated with less massive evolved stars. These stars, however, contribute much less to the transient detection rate than BSGs/RSGs, given their lower intrinsic brightnesses as shown in Fig. 1, which requires a higher (less likely) magnification.

As shown in Fig. 3, for a coeval stellar population having age  $> 10$  Myr, the transient detection rate decreases more slowly with age in the R than B filters. This means the  $B/R$  ratio decreases as a function of age as shown in Fig. 4. For a stellar population at the youngest age of  $\lesssim 3$  Myr, the detection rate is significantly higher in the blue filter, thus yielding a high  $B/R$  ratio of  $\sim 10^{2-3}$ . At such young ages, the DTM stars are mostly BSGs, as demonstrated by the blue isochrone in Fig. 1, while less massive stars need more time to evolve into the RSG phase. Although BSGs are so bright that they can sometimes be detected also in the red F200W filter, they primarily contribute to the detection rate in the blue filter, as shown in Fig. 3. On the other hand, red DTM stars (most likely, RSGs) only begin to appear at a slightly older age of  $\gtrsim 5$  Myr (the cyan isochrone in Fig. 1) as they are evolved stars that take time to get to this stage. The  $B/R$

ratio thus drops quickly once massive stars start to enter the RSG phase. At even older ages of  $\gtrsim 5 - 40$  Myr (depending on the metallicity/dust extinction), the most massive and thus brightest BSGs are gone, with few of the dimmer BSGs surviving as shown by the green isochrone in Fig. 1. RSGs, alongside other red evolved stars, are the only DTM stars that exist such that the  $B/R$  ratio falls below unity as reflected by both Fig. 3 and Fig. 4. This trend continues at even older stellar populations, where the  $B/R$  ratio fluctuates owing to effects related to metallicity and dust extinction.

The dependence of the  $B/R$  ratio on metallicity is less strong than that on age. As can be seen in Fig. 4, the  $B/R$  ratio decreases with increasing metallicity at ages up to  $\sim 100$  Myr, beyond which fluctuations arise owing to sampling noise. The main driver behind the dependence on metallicity is the metal absorption in stellar atmospheres, which is more abundant in the B than R filters. As shown by the isochrones in Fig. 1, stars with high metallicities (indicated by dotted lines) are cooler (thus redder) compared with those with lower metallicity (indicated by dashed lines). The trend of decreasing  $B/R$  ratio with increasing metallicity holds at all ages except  $\sim 10$  Myr when stars have supersolar metallicity, as can be seen in Fig. 4. At such high metallicities, the increase in stellar opacity owing to metal absorption inflates the star so as to lead to increased mass loss via a stellar wind (Vink, Jorick S. et al. 2001). With the outer envelope stripped away, the massive stars cannot evolve into RSGs and remain as BSGs, leading to a dip in the transient detection rate in the R filter at  $\sim 10$  Myr, therefore explaining the bump in the  $B/R$  ratio at this age at a metallicity of  $1.5Z_{\odot}$ .

Dust extinction also has a secondary effect on the  $B/R$  ratio compared with age. Increasing the dust extinction results in more blue light being scattered to longer wavelengths, making the observed stellar population redder in general. This increase leads to the detection of more red transients and suppresses the  $B/R$  ratio at any age. Such an effect is more prominent after an age of  $\sim 10$  Myr — the DTM stars at such age are much dimmer, and the dust extinction would make them even dimmer in the B filter, thus further lowering the  $B/R$  ratio.

Last but not least, we found that the  $B/R$  ratio varies relatively weakly with the IMF. We do not show the case for a top-heavy IMF in Fig. 4, as the changes induced compared with a Kroupa IMF are much weaker than the observed variation with age. A shallower IMF gives rise to more blue transients at ages less than 3 Myr, with a fractional change in the  $B/R$  ratio of  $\lesssim 20\%$ . This difference in the  $B/R$  ratio for the different stellar IMFs diminishes ( $\lesssim 3\%$ ) at older ages as Kroupa has a similar slope as the Top-heavy IMF for low- to intermediate-mass stars.

As proof-of-concept, we test how the  $B/R$  ratio provides a complementary constraint on the composition of a stellar population in addition to its observed spectral energy distributions (SEDs). The observed  $B/R$  ratio of the Warhol arc is  $0.62 \pm 0.35$  (4 F200LP transients in 2 *HST* epochs and 13 F200W transients in 4 *JWST* epochs, Kelly et al. 2022; Yan et al. 2023). Assuming that light from the Warhol arc is dominated by a coeval population of young stars, we deduce from Fig. 4 that this arc must have experienced a starburst  $\sim 5 - 40$  Myr ago, depending on the assumed metallicity. As we show in Fig. 5, however, the observed SED (black curve, from Palencia et al. 2025) is not consistent with a starburst over the aforementioned age range (the lowest reduced  $\chi^2$  being high as  $\sim 10^2$  as shown as the blue curve). Fitting a single starburst generated by SPISEA to the observed SED of Warhol, we find that the best-fit age is  $\sim 350$  Myr (requiring  $0.3Z_{\odot}$  and  $A_V = 0.9$ ) for which the reduced  $\chi^2$  is 2.8 (red curve in Fig. 5). The predicted  $B/R$  ratio of this best-fit model,



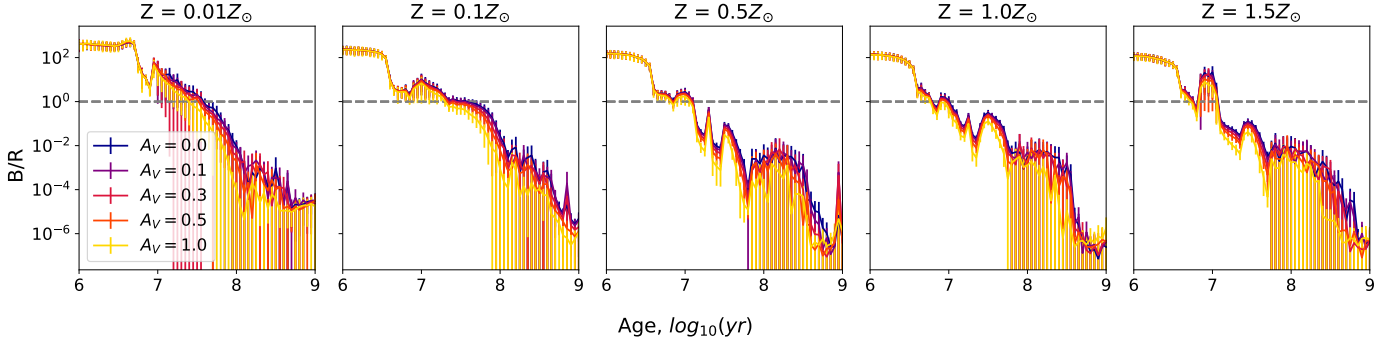


Fig. 4:  $B/R$  ratio calculated based on the F200LP and F200W transient detection rate in Warhol arc shown in Fig. A.1, with a Kroupa IMF. Each of the panels shows the case for one of the metallicities as indicated in the subtitles. The colour of each curve indicates the dust extinction. The gray dashed line denotes  $B/R = 1$  for reference. The  $1\sigma$  error bars are propagated from the sampling noise and the ten realizations of the stellar population for each combination of star formation parameters.

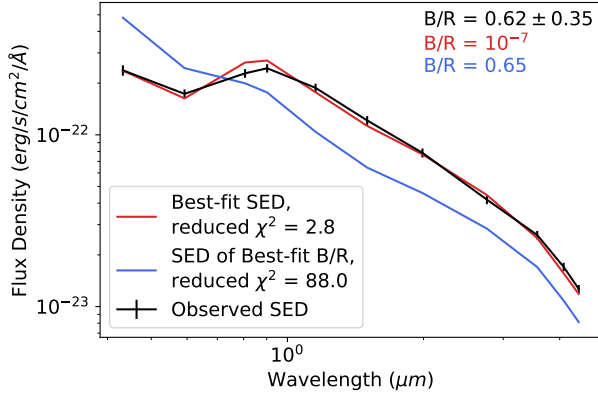


Fig. 5: SED of Warhol arc (black curve, from Palencia et al. 2025). The best fit (red curve) corresponds to a single star burst model at an age of  $\sim 350$  Myr with  $Z_{\star} = 0.3Z_{\odot}$  and  $A_V = 0.9$ . This model predicts  $B/R = 10^{-7}$ , orders of magnitude from the observed  $B/R = 0.62$ . Among all the models that can reproduce the observed  $B/R$  ratio well, we show the best fit SED as a blue curve. This model corresponds to a single star burst at an age of  $\sim 12$  Myr with  $Z_{\star} = 0.5Z_{\odot}$ , and  $A_V = 0.5$ . We adopted a Kroupa IMF in both models.

however, is of the order of  $10^{-7}$ , which clearly contradicts the observed  $B/R$  ratio. The corresponding Markov-Chain Monte-Carlo sampling of the aforementioned result in how the  $B/R$  ratio and SED constrain the single star burst model is shown in Figure B.1, where one can clearly see  $\sim 4\sigma$  tension between the age of the starburst inferred from the  $B/R$  ratio (blue contours) and SED (red contours), regardless of the choice of the IMF.

Our mock calculation demonstrates that the Warhol arc must have a more complicated star formation history to fit the SED and  $B/R$  ratio simultaneously. Demanding a simultaneous fit to both the  $B/R$  ratio and SED should help better constrain relevant galaxies' actual (recent) star formation history. A full exploration of such a simultaneous fit is deferred to a future paper.

## Acknowledgements

S.K.L. and J.L. acknowledge support from the Research Grants Council (RGC) of Hong Kong through the General Research Fund (GRF) 17302023. J.M.P. received financial support from the Formación de Personal Investigador (FPI) programme, ref.

PRE2020-096261, associated with the Spanish Agencia Estatal de Investigación project MDM-2017-0765-20-2. J.M.D. acknowledges support from project PID2022-138896NB-C51 (MCIU/AEI/MINECO/FEDER, UE) Ministerio de Ciencia, Investigación y Universidades.

We made use of the following software: Python, NumPy, Matplotlib, SciPy, Astropy, SPiSEA, emcee, and corner.

## References

- Chen, W., Kelly, P. L., Diego, J. M., et al. 2019, *ApJ*, 881, 8, doi: [10.3847/1538-4357/ab297d](#)
- Choi, J., Dotter, A., Conroy, C., et al. 2016, *ApJ*, 823, 102, doi: [10.3847/0004-637X/823/2/102](#)
- Diego, J. M. 2019, *A&A*, 625, A84, doi: [10.1051/0004-6361/201833670](#)
- Diego, J. M., Willner, S. P., Palencia, J. M., & Windhorst, R. A. 2024a, *arXiv e-prints*, arXiv:2410.09162, doi: [10.48550/arXiv.2410.09162](#)
- Diego, J. M., Meena, A. K., Adams, N. J., et al. 2023, *A&A*, 672, A3, doi: [10.1051/0004-6361/202245238](#)
- Diego, J. M., Li, S. K., Meena, A. K., et al. 2024b, *A&A*, 681, A124, doi: [10.1051/0004-6361/202346761](#)
- Diego, J. M., Li, S. K., Amruth, A., et al. 2024c, *A&A*, 689, A167, doi: [10.1051/0004-6361/202450474](#)
- Dohm-Palmer, R. C., & Skillman, E. D. 2002, *AJ*, 123, 1433, doi: [10.1086/339182](#)
- Eggenberger, P., Meynet, G., & Maeder, A. 2002, *A&A*, 386, 576, doi: [10.1051/0004-6361:20020262](#)
- Fudamoto, Y., Sun, F., Diego, J. M., et al. 2025, *Nature Astronomy*, 9, 428, doi: [10.1038/s41550-024-02432-3](#)
- Hosek, Jr., M. W., Lu, J. R., Lam, C. Y., et al. 2020, *AJ*, 160, 143, doi: [10.3847/1538-3881/aba533](#)
- Kelly, P. L., Diego, J. M., Rodney, S., et al. 2018, *Nature Astronomy*, 2, 334, doi: [10.1038/s41550-018-0430-3](#)
- Kelly, P. L., Chen, W., Alfred, A., et al. 2022, *arXiv e-prints*, arXiv:2211.02670, doi: [10.48550/arXiv.2211.02670](#)
- Kroupa, P. 2001, *MNRAS*, 322, 231, doi: [10.1046/j.1365-8711.2001.04022.x](#)
- Li, S. K., Diego, J. M., Kelly, P. L., et al. 2024, *arXiv e-prints*, arXiv:2404.08571, doi: [10.48550/arXiv.2404.08571](#)
- Li, S. K., Diego, J. M., Meena, A. K., et al. 2025, *arXiv e-prints*, arXiv:2504.06992, doi: [10.48550/arXiv.2504.06992](#)
- Meena, A. K., Chen, W., Zittrn, A., et al. 2023, *MNRAS*, 521, 5224, doi: [10.1093/mnras/stad869](#)
- Miralda-Escude, J. 1991, *ApJ*, 379, 94, doi: [10.1086/170486](#)
- Oguri, M., Diego, J. M., Kaiser, N., Kelly, P. L., & Broadhurst, T. 2018, *Phys. Rev. D*, 97, 023518, doi: [10.1103/PhysRevD.97.023518](#)
- Oke, J. B., & Gunn, J. E. 1983, *ApJ*, 266, 713, doi: [10.1086/160817](#)
- Palencia, J. M., Diego, J. M., Kavanagh, B. J., & Martínez-Arrizabalaga, J. 2024, *A&A*, 687, A81, doi: [10.1051/0004-6361/202347492](#)
- Palencia, J. M., Diego, J. M., Dai, L., et al. 2025, *arXiv e-prints*, arXiv:2504.07039, doi: [10.48550/arXiv.2504.07039](#)
- Vink, Jorick S., de Koter, A., & Lamers, H. J. G. L. M. 2001, *A&A*, 369, 574, doi: [10.1051/0004-6361:20010127](#)
- Williams, H. in prep.
- Windhorst, R. A., Cohen, S. H., Jansen, R. A., et al. 2023, *AJ*, 165, 13, doi: [10.3847/1538-3881/aca163](#)
- Yan, H., Ma, Z., Sun, B., et al. 2023, *ApJS*, 269, 43, doi: [10.3847/1538-4365/ad0298](#)

## Appendix A: All simulated cases

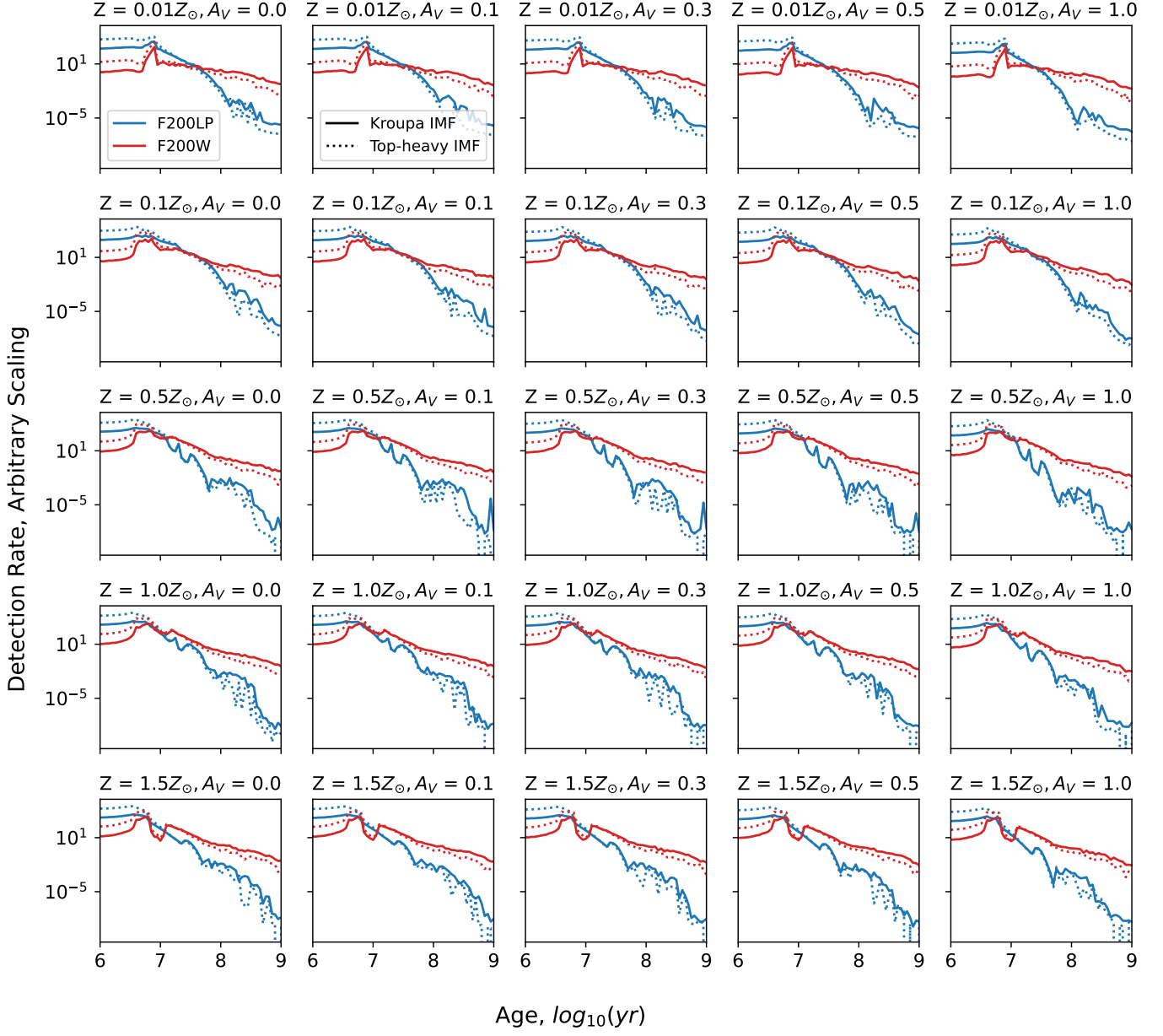


Fig. A.1: Same as Fig. 3, but for the cases with different metallicities and dust extinction as denoted in the subtitles of each of the panels. We do not show the error bar for clarity issues.

## Appendix B: MCMC analysis

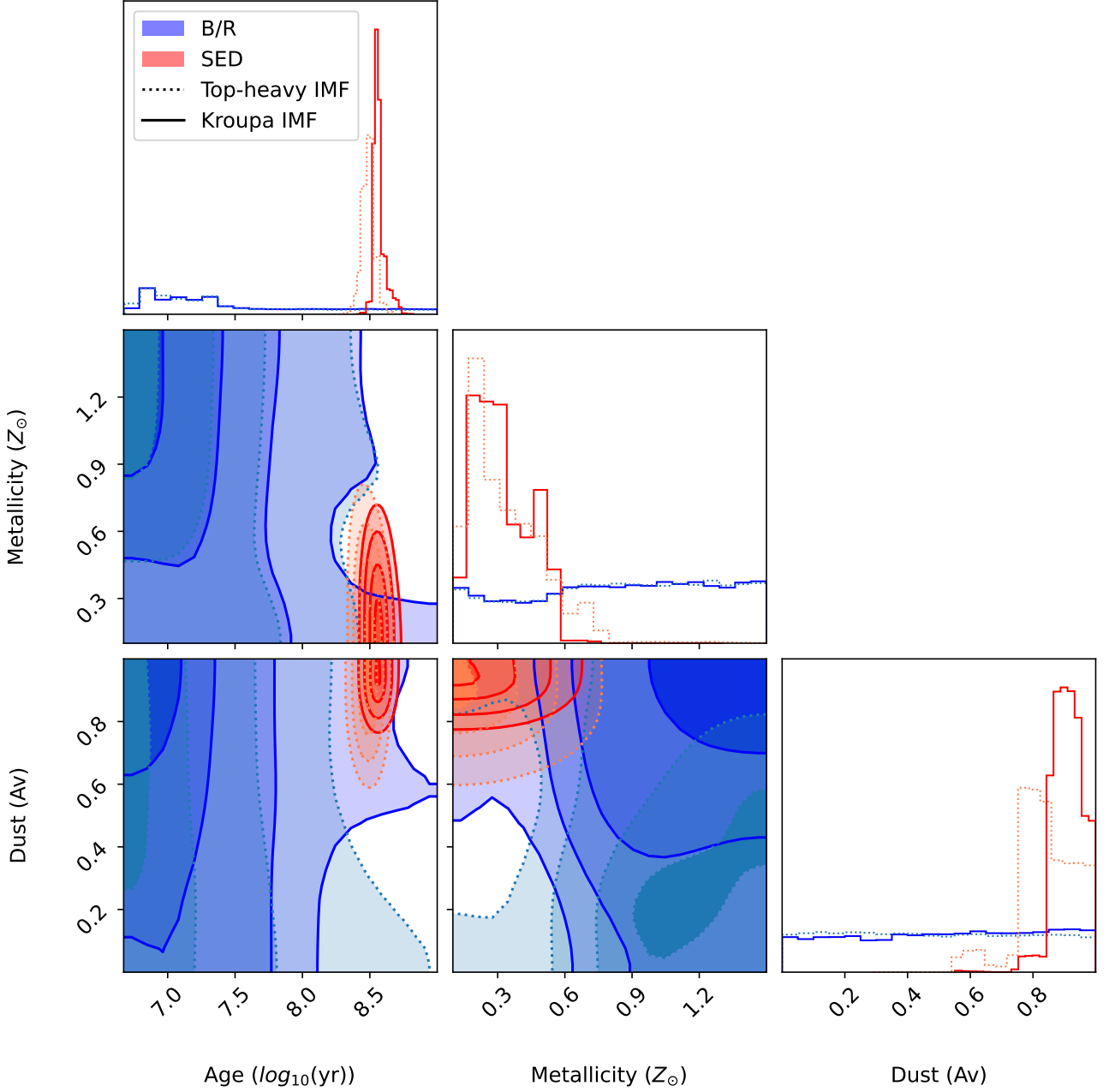


Fig. B.1: Markov-Chain Monte-Carlo analysis regarding the constraining power of  $B/R$  (blue) and SED (red) of Warhol on the parameter space, given that we assume there is only one single burst of star formation at age  $t$  with metallicity  $Z_{\star}$  and dust extinction  $A_V$ . Since we only care about the inference of these three parameters, all the SED templates generated by SPISEA are pre-normalized to best fit the observed SED of Warhol. The contour levels correspond to  $1 - 4\sigma$  level confidences. Histograms/contours in solid lines represent the case for a Kroupa IMF, where those in dotted lines (with a slight color tweak to improve visibility) represent the case for a Top-heavy IMF. There is no significant difference in preference for star formation parameters constrained by either  $B/R$  or SED when a different IMF is adopted.